

Letter

Distribution and Evolution of Metals in the *Magneticum* simulations

Klaus Dolag^{1,2}, Emilio Mevius¹, and Rhea-Silvia Remus¹

¹ Universitäts-Sternwarte München, Scheinerstr. 1, D-81679 München, Germany

² Max Planck Institut for Astrophysics, D-85748 Garching, Germany

* dolag@usm.lmu.de

Academic Editor: name

Version July 28, 2017 submitted to *Galaxies*

Abstract: Metals are ideal tracers of the baryonic cycle within halos. Their composition is a fossil record connecting the evolution of the various stellar components of galaxies to the interaction with the environment by in- and outflows. The *Magneticum* simulations allow to study halos across a large range of masses and environments, from massive galaxy clusters containing hundreds of galaxies down to isolated field galaxies. They include a detailed treatment of the chemo-energetic feedback from the stellar component and its evolution as well as feedback from the evolution of supermassive black holes. Following the detailed evolution of various metal species and their relative composition due to continuing enrichment of the IGM and ICM by SNIa, SNII and AGB winds of the evolving stellar population reveals the complex interplay of local star formation processes, mixing, global baryonic flows, secular galactic evolution and environmental processes. We present results from the *Magneticum* simulations on the chemical properties of simulated galaxies and galaxy clusters, carefully comparing them to observations. We show that the simulations already reach a very high level of realism within their complex descriptions of the chemo-energetic feedback, successfully reproducing a large number of observed properties and scaling relations. Our simulated galaxies clearly indicate that there are no strong secondary parameters (like star formation rates at fixed redshift) driving the scatter in these scaling relations. The remaining differences clearly point to detailed physical processes which have to be included into future simulations.

Keywords: Galaxy clusters – intra cluster medium – galaxies – stellar population – numerical simulation

1. Introduction

In cosmological hydrodynamical simulations, star formation is typically treated based on a sub-grid model. Star particles are formed when the gas locally exceeds a certain density threshold, when it is Jeans unstable, and the local gas flow converges at a gas particle. Each star particle represents a simple stellar population which is characterized by an initial mass function (IMF).

In addition, each star particle emits a feedback that is mimicking the winds which are launched by stars in reality by averaging over the whole stellar population included in each simulated stellar particle. In most models, the considered winds compose of three main stellar sources: Supernovae Type II (SNII), Supernovae Type Ia (SNIa), and asymptotic giant branch stars (AGBs). These three sources are considered to be the most important drivers of observed stellar outflows and thus the main contributors to metal enrichment of the interstellar medium:

Stars with masses larger than $8 M_{\odot}$ are believed to end their lives through a so called core collapse (SNII), releasing typically an energy of 10^{51} erg per supernova together with their chemical imprint into the surrounding gas. These supernovae usually occur shortly after the formation of the simulated star

34 particle, as the most massive stars only live for a short time and thus this part of the stellar population
 35 of the star particle is emitting first. SNIa on the other hand are believed to arise from thermonuclear
 36 explosions of white dwarfs within binary stellar systems. These supernovae are delayed relatively
 37 to the SNII and occur later in a star particle's live, as the white dwarf in the according binary system
 38 has to first be formed and second needs to accrete matter from its companion until it reaches the mass
 39 threshold for the onset of thermonuclear burning. Therefore, a detailed modelling of the evolution of
 40 the stellar population has to be included in the simulations to follow the chemo-energetic imprint of
 41 the SNIa on the surrounding gas. AGB stars contribute emitting strong winds, exhibiting strong mass
 42 losses during their life and are importantly contributing to the nucleosynthesis of heavy elements.

43 To include the effects of these sources into the sub-grid models of simulated stellar particles
 44 raises the need to integrate a set of complicated equations describing the evolution of a simple stellar
 45 population. Such set of integral equations then allows to compute at each time the rate at which the
 46 current AGB stars pollute their environment by stellar winds and the rate at which the SNIa and SNII
 47 are exploding. Such they allow to properly treat the chemo-energetic imprint on the surrounding
 48 inter-galactic medium (IGM) and the inter-cluster medium (ICM). In the following we will give a
 49 short, schematic description of such calculations based on the description presented in Dolag et al.,
 50 (2017) [1] (for a more detailed review, see Matteucci 2003 [2] and Borgani et al. 2008 [3], and references
 51 therein). Then we will introduce the cosmological hydrodynamical simulation set used in this work,
 52 and present a comparison of the metal enrichment in galaxies and clusters of galaxies caused by
 53 this model feedback with observations. Finally, we will summarize and discuss the results of this
 54 comparison in the light of model improvements needed for the future.

55 2. Chemical Enrichment

56 To describe the continuous enrichment of the IGM and ICM through winds from SNIa, SNII
 57 and AGB stars in the evolving stellar population of each star particle, several ingredients are needed.
 58 In the following we will shortly present the ingredients used in many state-of-the-art cosmological
 59 simulations of galaxy formation.

60 2.1. IMF

61 One of the most important quantities in models of chemical evolution is the IMF. It directly
 62 determines the relative ratio between SNII and SNIa, and therefore the relative abundance of α -elements
 63 and Fe-peak elements. The shape of the IMF also determines the ratio between low-mass long-living
 64 and massive short-living stars. This ratio directly affects the amount of energy released by the SNe
 65 as well as the present luminosity of galaxies which is dominated by low mass stars and the (metal)
 66 mass-locking in the stellar phase.

The IMF $\phi(m)$ describes the number of stars of a given mass per unit logarithmic mass interval.
 Historically, a commonly used form is the Salpeter IMF (Salpeter 1955 [4]) which follows a single
 power-law with an index of $x = 1.35$. However, different expressions of the IMF have been proposed
 more recently in order to model a flattening in the low-mass regime of the stellar mass function that is
 currently favoured by a number of observations. Among the newer, often used models is the Chabrier
 IMF (Chabrier 2003 [5]), which has a continuously changing slope and is more top heavy than the
 Salpeter IMF:

$$\phi(m) \propto \begin{cases} m^{-1.3} & m > 1 M_{\odot} \\ e^{\frac{-(\log(m)-\log(m_c))^2}{2\sigma^2}} & m \leq 1 M_{\odot} \end{cases} \quad (1)$$

67 However, the question of whether there is a global IMF or if the IMF is changing with galaxy mass,
 68 morphology or cosmological time, and which IMF has to be chosen is still an unsolved problem and a
 69 matter of heavy debate.

70 2.2. Lifetime functions

To model the evolution of a simple stellar population, a detailed knowledge of the lifetimes of stars with different masses is required. Different choices for the mass-dependence of the lifetime function have been proposed in the literature (e.g. Padovani and Matteucci (1993) [6], Maeder and Meynet (1989) [7], Chiappini et al., (1997) [8]), where the latest one reads:

$$\tau(m) = \begin{cases} 10^{-0.6545 \log m + 1} & m \leq 1.3 M_{\odot} \\ 10^{-3.7 \log m + 1.351} & 1.3 < m \leq 3 M_{\odot} \\ 10^{-2.51 \log m + 0.77} & 3 < m \leq 7 M_{\odot} \\ 10^{-1.78 \log m + 0.17} & 7 < m \leq 15 M_{\odot} \\ 10^{-0.86 \log m - 0.94} & 15 < m \leq 53 M_{\odot} \\ 1.2 \times m^{-1.85} + 0.003 & \text{otherwise.} \end{cases} \quad (2)$$

71 2.3. Stellar Yields

72 The ejected masses of the different metal species i produced by a star of mass m are called stellar
73 yields $p_{Z_i}(m, Z)$. These yields depend on the metallicity Z with which the star originally formed, and
74 on the type of outflow ejected from the star. Therefore, detailed predictions for the main three sources
75 of enrichment are needed, namely for the mass loss of AGB stars, of SNII, and of SNIa. Up to date,
76 such predictions still suffer from significant uncertainties, mainly due to the still poorly understood
77 mass loss through stellar winds in stellar evolution models, which depends on multiple additional
78 physical processes.

79 For the mass loss through AGB stars, the most recent predictions can be found in Karakas (2007) [9].
80 Predictions for the mass loss from massive stars driving SNII are presented by Nomoto, Kobayashi
81 & Tominaga (2013) [10]. The most complete table for SNIa up to date is presented by Thielmann
82 (2003) [11].

83 2.4. Modelling the Enrichment Process

84 As summarized by Dolag (2017) [1], the assumption of a generic star formation history represented
85 by an arbitrary function of time $\psi(t)$ allows to compute the rates for the different contributions in
86 form of a set of integral equations as shown in the following (for more details, see also Matteucci
87 2003 [2], Borgani et al. 2008 [3], and references therein). This formalism can be individually applied to
88 the large number of particles representing the continuous star-formation process within cosmological
89 simulations. Every star particle here represents a stellar population born in a single burst. The
90 combination of all the stellar component within the simulated galaxies results then in a model which
91 describes the legacy of the detailed star-formation history of any simulated galaxy.

92 2.4.1. Type Ia supernovae

SNIa occur in binary systems with masses in a mass range of $0.8\text{--}8 M_{\odot}$. Let m_B be the total mass of the binary system and m_2 the mass of the secondary companion. We can now use $f(\mu)$ as the distribution function of binary systems with $\mu = m_2/m_B$ and define A as the fraction of stars in binary systems that are progenitors of SNIa. Therefore, A has to be given or obtained by a model. Constructing such detailed models for SNIa progenitors is particular difficult, see for example Greggio & Renzini (1983) [12] or Greggio (2005) [13]. Based on such kind of models, typical value for A are inferred to be in the range of 0.05 and 0.1, based on comparisons of chemical enrichment models with observed iron metallicities within galaxy clusters (e.g. Matteucci & Gibson 1995 [14]) or within the solar neighbourhood (e.g. Matteucci & Greggio 1986 [15]). Within the current simulations we are using

a value of $A = 0.1$. With these ingredients and the mass dependent lifetime functions $\tau(m)$, we can model the rate of SNIa as

$$R_{\text{SNIa}}(t) = A \int_{M_{\text{B,inf}}}^{M_{\text{B,sup}}} \phi(m_{\text{B}}) \int_{\mu_{\text{m}}}^{\mu_{\text{M}}} f(\mu) \psi(t - \tau_{m_2}) d\mu dm_{\text{B}}. \quad (3)$$

93 where M_{Bm} and M_{BM} are the smallest and largest values, respectively, that are allowed for the
 94 progenitor binary mass m_{B} . Then, the integral over m_{B} runs in the range between $M_{\text{B,inf}}$ and $M_{\text{B,sup}}$,
 95 which represent the minimum and the maximum value of the total mass of the binary system that is
 96 allowed to explode at the time t . These values in general are functions of M_{Bm} , M_{BM} , and $m_2(t)$, which
 97 in turn depend on the star formation history $\Psi(t)$. In simulations, where the individual stellar particles
 98 are in commonly modelled as an impulsive star formation event, $\psi(t)$ can therefore be approximated
 99 with a Dirac δ -function. The sum of all stellar particles and their individual formation time then
 100 represent the complex star-formation history of the galaxies within the simulation.

101 2.4.2. Supernova Type II, Low-, and Intermediate-mass stars

Computing the rates of SNII, low-mass stars (LMS), and intermediate-mass stars (IMS) is conceptually simpler than calculating the rates of SNIa, since they are purely driven by the lifetime function $\tau(m)$ convolved with the star formation history $\psi(t)$ and multiplied by the IMF $\phi(m = \tau^{-1}(t))$. Since $\psi(t)$ is a delta-function for the simple stellar populations used in simulations, the SNII, LMS and IMS rates read

$$R_{\text{SNII|LMS|IMS}}(t) = \phi(m(t)) \times \left(-\frac{dm(t)}{dt} \right) \quad (4)$$

102 where $m(t)$ is the mass of the star that dies at time t . For AGB rates, the above expression must be
 103 multiplied by a factor of $(1 - A)$ if the mass $m(t)$ falls in the range of masses which is relevant for the
 104 secondary stars of SNIa binary systems.

105 2.4.3. The equations of chemical enrichment

106 In order to compute the total metal release from the simple stellar population, we have to fold the
 107 above rates with the yields $p_{Z_i}^{\text{SNIa|SNII|AGB}}(m, Z)$ from SNIa, SNII and AGB stars for a given element
 108 i for stars born with initial metallicity Z_i , and compute the evolution of the density $\rho_i(t)$ for each
 109 element i at each time t . As shown in Borgani et al., (2008) [3], this reads

$$\dot{\rho}_i(t) = - \psi(t) Z_i(t) \quad (5)$$

$$+ \int_{M_{\text{BM}}}^{M_{\text{U}}} \psi(t - \tau(m)) p_{Z_i}^{\text{SNII}}(m, Z) \phi(m) dm \quad (6)$$

$$+ A \int_{M_{\text{Bm}}}^{M_{\text{BM}}} \phi(m) \left[\int_{\mu_{\text{m}}}^{\mu_{\text{M}}} f(\mu) \psi(t - \tau_{m_2}) p_{Z_i}^{\text{SNIa}}(m, Z) d\mu \right] dm \quad (7)$$

$$+ (1 - A) \int_{M_{\text{Bm}}}^{M_{\text{BM}}} \psi(t - \tau(m)) p_{Z_i}^{\text{AGB}}(m, Z) \phi(m) dm \quad (8)$$

$$+ \int_{M_{\text{L}}}^{M_{\text{Bm}}} \psi(t - \tau(m)) p_{Z_i}^{\text{AGB}}(m, Z) \phi(m) dm, \quad (9)$$

110 where M_{L} and M_{U} are the minimum and maximum mass of a star in the simple stellar population,
 111 respectively. Commonly adopted choices for these limiting masses are $M_{\text{L}} \simeq 0.1 M_{\odot}$ and $M_{\text{U}} \simeq$
 112 $100 M_{\odot}$.

113 In the above equation, the first line describes the locking of metals in new born stars through the
 114 currently ongoing star formation $\psi(t)$, which for the assumed sub-grid model case vanishes as $\psi(t)$ is

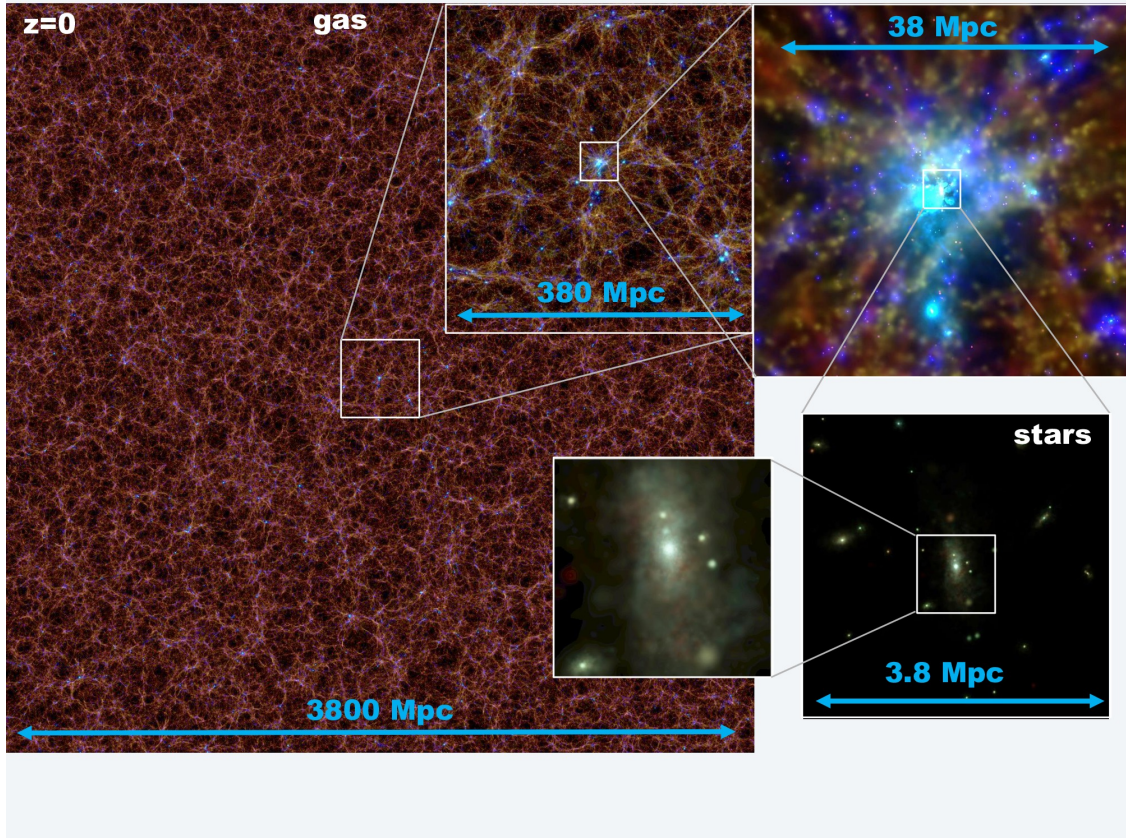


Figure 1. Visualization of the large scale distribution of the gas and stellar component within *Box0* (see Bocquet et al., 2016 [17]) of the *Magneticum* simulation set at redshift $z = 0$. The inlays show a consecutive zoom onto the most massive galaxy cluster, where the individual galaxies become visible.

115 a delta function. For a comprehensive review of the analytic formalism we refer the reader to Greggio
 116 (2005) [16].

117 3. The *Magneticum* Simulations

118 The *Magneticum* simulation set covers a huge dynamical range, from very large cosmological
 119 volumes as shown in Fig. 1, which can be used for statistical studies of clusters and voids (e.g.
 120 Bocquet et al. 2016 [17], Pollina et al. 2017 [18]), to very high resolution simulations of smaller
 121 cosmological volumes which allow a morphological classification and a detailed analysis of galaxies
 122 and their properties (e.g. Teklu et al. 2015 [19] and Remus et al. 2017 [20]). Table 1 lists the detailed
 123 properties like size and stellar mass-resolution of the different simulations. These simulations treat the
 124 metal-dependent radiative cooling, heating from a uniform time-dependent ultraviolet background,
 125 star formation and the chemo-energetic evolution of the stellar population as traced by SNIa, SNI

Table 1. Size and number of particles for the different simulations. The last two rows list the average mass and softening of the star particles for the different resolution levels.

Simulation	Box0	Box1	Box2b	Box2	Box3	Box4	m_{star}	ϵ_{star}
Size [Mpc]	3820	1300	910	500	180	68	$[M_{\odot}]$	[kpc]
mr	2×4536^3	2×1512^3	–	2×594^3	2×216^3	2×81^3	6.5×10^8	5
hr	–	–	2×2880^3	2×1564^3	2×576^3	2×216^3	3.5×10^7	2
uhr	–	–	–	–	2×1536^3 ($z=2$)	2×576^3	1.9×10^6	0.7

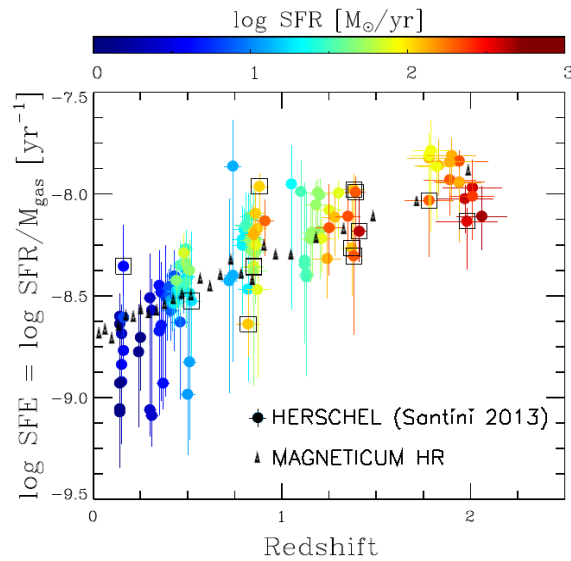


Figure 2. Redshift evolution of the SFE (coloured points with error bars) from Herschel observations presented by Santini et al., (2014) [23] overlaid with the predicted median values at different redshifts from star forming galaxies in the *Magneticum* simulations (black triangles).

126 and AGB stars with the associated feedback processes and stellar evolution details as described before.
 127 They also include the formation and evolution of super-massive black holes and the associated quasar
 128 and radio-mode feedback processes. For a detailed description of the simulation sample see Dolag et
 129 al. (in prep), Hirschmann et al. (2014) [21], and Teklu et al. (2015) [19].

130 4. Metallicities from *Magneticum* in Comparison to Observations

131 As previously shown from re-simulations of massive galaxy clusters, the observed radial profiles
 132 of Iron within the ICM can be well reproduced in simulations: Biffi et al., (2017) [22] demonstrated that
 133 especially at high redshifts the implemented AGN feedback is the main driver in enhancing the metal
 134 enrichment in the ICM at large cluster-centric distances to the observed level.

135 The *Magneticum* simulations now allow such investigations across a much larger range of halo
 136 masses. For this study we use a large simulation volume (Box2 hr) with enough resolution to
 137 resolve mean properties of galaxies (and AGNs), resulting in the same resolution as used in Biffi
 138 et al., (2017) [22] and Hirschmann et al., (2014) [21]. For galaxies, the star formation efficiency
 139 (SFE) is a measure of the SFR per unit of gas mass. To evaluate whether the SF activity in the
 140 simulations match the observational data is a key step to proceed towards reproducing the observed
 141 mass-metallicity-relation (MZR). In Fig. 2, the evolution of the observed SFE up to a redshift of $z \approx 2$
 142 is shown in comparison to the evolution of the SFE of star forming galaxies in *Magneticum*. As can
 143 clearly be seen, the simulations are in excellent agreement with the observed trends up to $z \approx 2$.

144 4.1. Galaxy Clusters: ICM Metallicities

145 X-ray observations of the intra cluster medium allow for a detailed study of the distribution
 146 of different metal species within the ICM via their line emissions within the X-ray band. Here, the
 147 composition of the individual metal species allows to interpret their abundances as an imprint of the
 148 relative contributions to the enrichment from SNIa and SNII, hence keeping a record on when and
 149 where these metals are injected into the ICM (e.g. De Plaa et al., 2007 [24]). The lower left panel of
 150 Fig. 3 shows a comparison of such observational data for various individual galaxy clusters with

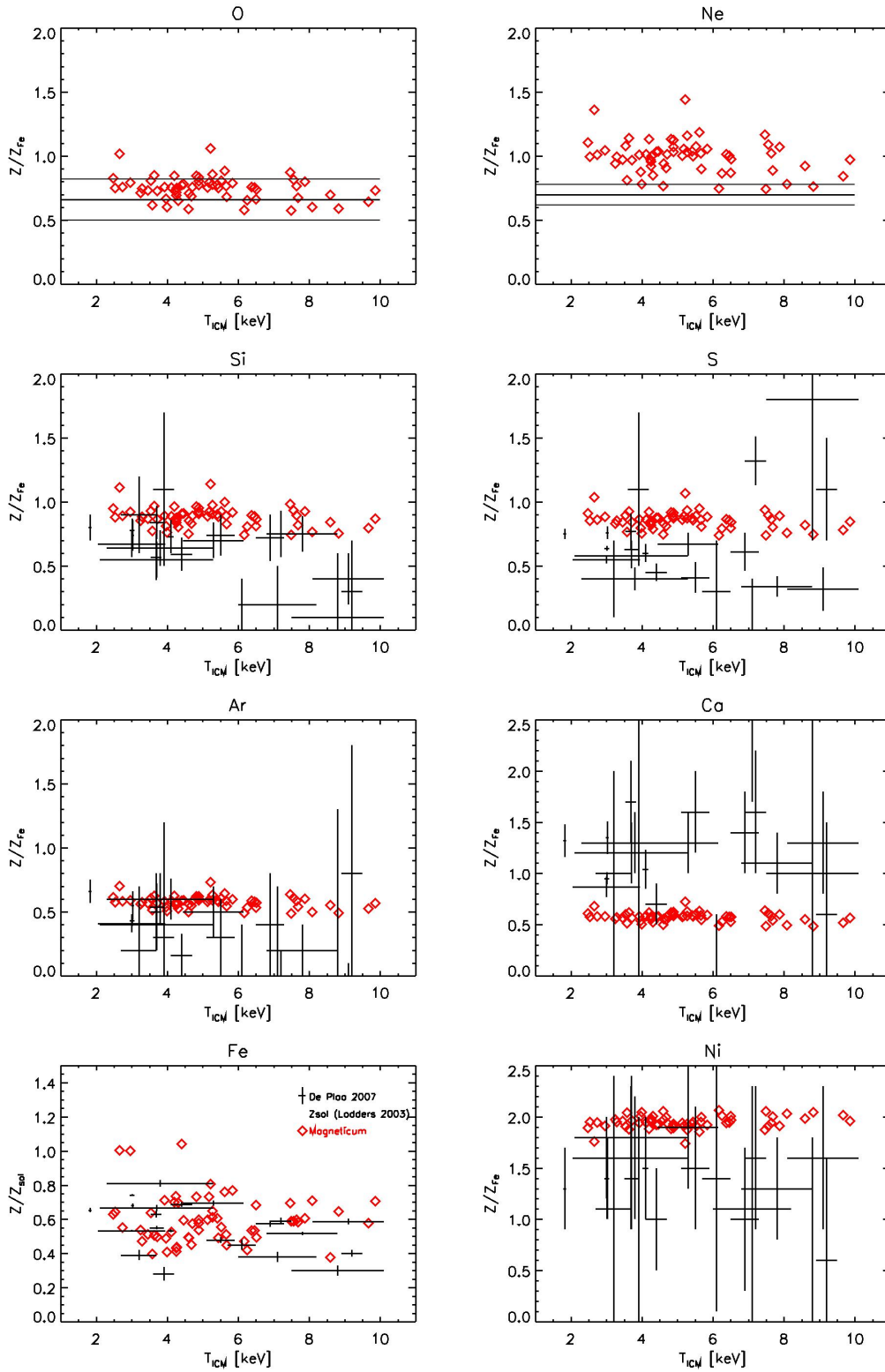


Figure 3. Comparison between the observed ICM metallicity within R_{2500} (black symbols with error bars) and the metallicities of galaxy clusters from the *Magneticum* simulations (red diamonds) as function of the ICM temperature. Different panels show the ratios for different metal types, as indicated in the panels. From top left to bottom right the relative contribution of SNIa is expected to increase, while the relative contribution of SNIId is expected to decrease. Observational data are taken from De Plaa et al. (2007) [24].

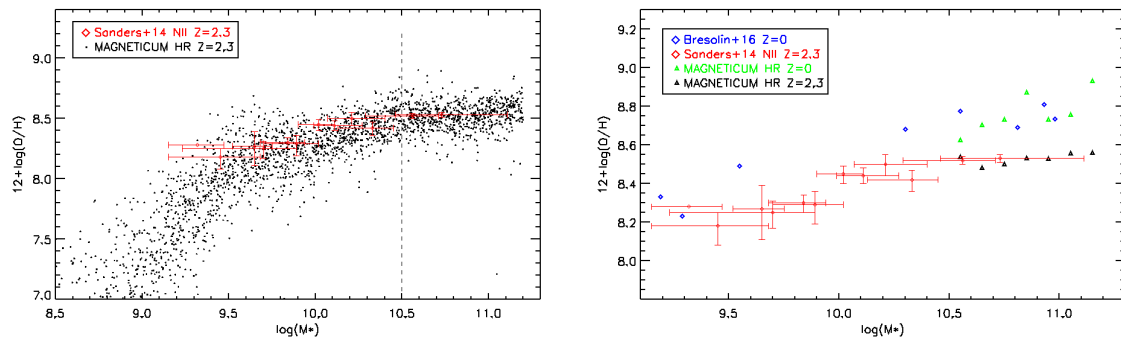


Figure 4. Gas-phase metallicity from *Magneticum* galaxies in comparison to observational data by Sanders et al. (2015) [26] at redshift $z = 2.3$ (red datapoints with error bars) and Bresolin et al. (2016) [27] at redshift $z = 0$ (blue diamonds). *Left panel:* Each black point represents a galaxy from the simulation. *Right panel:* Median values for each mass bin at $z = 2.3$ (black) and $z = 0$ (green) are shown as triangles.

151 simulations, clearly demonstrating the ability of the *Magneticum* simulations to reproduce the correct
 152 absolute iron abundance within the ICM self-consistently.

153 Here the scatter of the absolute iron abundance within the simulated clusters shows a similar
 154 spread (factor of two) as the observed values with a very mild trend of increasing iron abundance for
 155 low mass (e.g. lower ICM temperature) clusters. In addition the simulations also reproduce broadly
 156 the chemical composition footprint of various elements species, as shown in the various panels. This
 157 strongly indicates that the simulations predict the correct ratio between the contributions to the metal
 158 enrichment from SNIa and SNII and its interplay with the AGN feedback. The simulations also predict
 159 typically less spread in the composition of the metals for the individual clusters than they show in their
 160 absolute iron metallicity.

161 4.2. Galaxies: Gas Metallicities

162 To estimate the gas phase metallicity of galaxies, it is important consider that observationally the
 163 measurements are obtained only from star forming regions. Therefore, it can be misleading to only
 164 calculate the mean metallicity of all gas particles inside a simulated galaxy. Thus, after selecting star
 165 forming galaxies (see Teklu et al. 2017 [25]) we can either calculate their mean metallicity by averaging
 166 over all particles which are currently star-forming, or alternatively calculate the mean metallicity of
 167 the new-born stars. We tested both methods and found that the latter gives slightly better results due
 168 to the fact that it is difficult to catch the metallicity of the gas phase in the moment of star formation
 169 within simulations given the large timespan between the simulation outputs, while the young stellar
 170 population freezes the record of the metallicity of the gas from which it was formed. This leads to
 171 a MZR which is in good agreement with observations, as shown in the left panel of Fig. 4, where
 172 we use the predicted Oxygen abundances from our calculations to be consistent with observations
 173 (Sanders et al. 2015 [26] at $z = 2.3$ and Bresolin et al. 2016 [27] at $z = 0$). Interestingly, even the
 174 overall evolution of the MZR is well captured by the simulations and matches the observations, as
 175 demonstrated in the right panel of Fig. 4. However, when calculating gas-phase metallicity gradients
 176 within the galaxies, the simulations predict a steeper profile than the observations. Given that the
 177 prediction of the mean metallicities is in good agreement with observations this indicates that the
 178 simulations either still lack the resolution to properly describe the mixing of the enriched gas within
 179 galaxies, or that on these scales the diffusion of metals might have to be modelled more explicitly.
 180 Nevertheless, we clearly showed that including detailed modelling of the stellar population combined
 181 with current AGN feedback models significantly improve the predicted ICM and IGM metallicities
 182 and are needed to successfully reproduce various aspects of the observations.

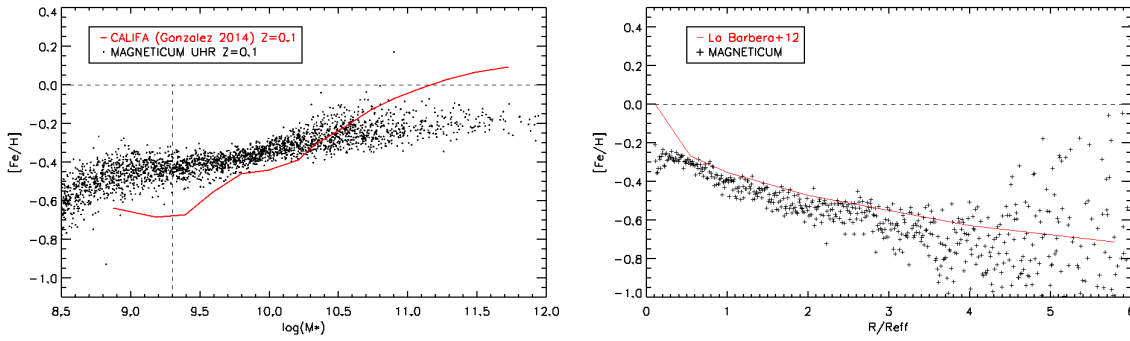


Figure 5. *Left panel:* Stellar metallicity versus stellar mass obtained from the *Magneticum* galaxies (black dots) in comparison with observational data for galaxies independent of their morphology from Gonzalez Delgado et al. (2014) [28] at redshift $z = 0$. *Right panel:* Mean stellar radial metallicity gradient from 100 *Magneticum* galaxies in 100 radial bins normalized to the half-mass radius (black dots) compared to the observed profile from La Barbera et al. (2012) [31], red line.

183 4.3. Galaxies: Stellar Metallicities

184 In general, we assume that the mean metallicity of a stellar particle in the simulation represents
 185 the mean stellar metallicity of the stellar population represented by the stellar particle, neglecting
 186 any self-enrichment within stars. To be consistent with the observations, we based all calculations
 187 on the Iron abundance as predicted by the simulations. For this part of the study we used a smaller
 188 cosmological volume with a higher resolution, as this allows a classification of the galaxies due
 189 to their morphological type (see Teklu et al. 2015 [19]) for more details on the classification and
 190 this particular simulation). This higher resolution also allows for a more detailed resolution of the
 191 metallicity gradients with radius for individual galaxies.

192 Although the obtained mean metallicities of our galaxies are close to observational results, the
 193 stellar MZR obtained from the simulations is somewhat shallower than the one obtained from CALIFA
 194 observations by Gonzalez Delgado et al. (2014) [28], as shown in the left panel of Fig. 5. This again
 195 indicates that the treatment of the mixing between accreted, more pristine material from outside the
 196 galaxy and the enriched gas within the galaxies is not fully captured yet. At this point it is unclear
 197 whether that will be resolved by further enhancing the resolution of simulations or whether explicit
 198 diffusion of metals has to be taken into account.

199 For a proper comparison of the radial metallicity gradients between simulations and observational
 200 data, it is necessary to calculate the effective radius R_{eff} for each galaxy. This is done by selecting all
 201 stellar particles within ten percent of the virial radius and then inferring the according half-mass radius,
 202 which we associate to the effective radius R_{eff} . This method has already been used to demonstrate that
 203 the *Magneticum* simulations successfully reproduce the mass-radius relation of galaxies for different
 204 morphological types (e.g. Remus et al. 2015 [29]) and at different redshifts (e.g. Remus et al. 2017 [20]).

205 Interestingly, the radial stellar metallicity gradients obtained from the simulations very well match
 206 the CALIFA observations, as shown in the right panel of Fig. 5. Note also that the increasing spread
 207 towards larger radius is an intrinsic, point-by-point spread within the individual galaxies and agrees
 208 well with the behaviour measured for individual galaxies by Pastorello et al. (2014) [30]. However,
 209 while the simulations successfully reproduce the observed Iron abundances and radial gradients, they
 210 still produce a flat ratio of Oxygen (or Magnesium or Silicon) over Iron, in contrast to the observations,
 211 and here the sub-grid model clearly needs to be advanced.

212 5. Discussion and Conclusion

213 Metals are measured in all phases of the baryonic universe, starting from the ICM in galaxy
214 clusters down to gas and stars in individual galaxies. As the radial distribution of different types
215 of metals encode a record of the star formation process over the whole time of a galaxies' evolution,
216 comparing the chemical footprint as seen in simulations with observations reflects an excellent test
217 on the reliability of the numerical sub-grid models included in modern state-of-the-art simulations of
218 galaxy formation in a cosmological context in reproducing the complex processed enrolled in galaxy
219 formation.

220 We demonstrated that the *Magneticum* simulations are able to reproduce a large variety of
221 observational findings over a large range of halo masses, indicating that the star-formation and
222 feedback processes included start to be highly realistic. At galaxy cluster scale the simulations show
223 an excellent agreement with both, the absolute value as well as the cluster by cluster variation of the
224 the iron abundance when comparing to x-ray observations and also reproduce broadly the chemical
225 composition of the ICM. On galaxy scales the tight mass-metallicity-relations found for our simulated
226 galaxies indicate that there are no strong secondary parameters (like star formation rates at fixed
227 redshift) driving the scatter in these relations. The remaining differences between the observed
228 properties and the simulation results indicate, however, that the incorporation of physical processes
229 like diffusion and mixing have to be improved within the next generation of simulations to successfully
230 reproduce the detailed distribution of metals on individually resolved galaxy scales.

231 **Acknowledgments:** The *Magneticum* Pathfinder simulations were performed at the Leibniz-Rechenzentrum
232 with CPU time assigned to the Projects "pr86re" and "pr83li". This work was supported by the DFG Cluster
233 of Excellence "Origin and Structure of the Universe". We are especially grateful for the support by M. Petkova
234 through the Computational Center for Particle and Astrophysics (C2PAP).

235 **Author Contributions:** K.D. performed the simulation and wrote the paper; E.M. analysed the data; R.-S.R.
236 contributed to the physical interpretation of the results, supervising E.M. during his master and to the writing of
237 the paper.

238 **Conflicts of Interest:** The authors declare no conflict of interest.

239 References

- 240 [1] Dolag, K. *Hydrodynamic methods for cosmological simulations*; Vol. 2, 2017.
- 241 [2] Matteucci, F. *The Chemical Evolution of the Galaxy*; 2003.
- 242 [3] Borgani, S.; Fabjan, D.; Tornatore, L.; Schindler, S.; Dolag, K.; Diaferio, A. The Chemical Enrichment of the
243 ICM from Hydrodynamical Simulations. *Space Sci. Rev.* **2008**, *134*, 379–403, [0801.1062].
- 244 [4] Salpeter, E.E. The Luminosity Function and Stellar Evolution. *ApJ* **1955**, *121*, 161.
- 245 [5] Chabrier, G. Galactic Stellar and Substellar Initial Mass Function. *PASP* **2003**, *115*, 763–795,
246 [astro-ph/0304382].
- 247 [6] Padovani, P.; Matteucci, F. Stellar Mass Loss in Elliptical Galaxies and the Fueling of Active Galactic Nuclei.
248 *ApJ* **1993**, *416*, 26.
- 249 [7] Maeder, A.; Meynet, G. Grids of evolutionary models from 0.85 to 120 solar masses - Observational tests
250 and the mass limits. *A&A* **1989**, *210*, 155–173.
- 251 [8] Chiappini, C.; Matteucci, F.; Gratton, R. The Chemical Evolution of the Galaxy: The Two-Infall Model. *ApJ*
252 **1997**, *477*, 765–780, [astro-ph/9609199].
- 253 [9] Karakas, A.; Lattanzio, J.C. Stellar Models and Yields of Asymptotic Giant Branch Stars. *PASA* **2007**,
254 *24*, 103–117, [0708.4385].
- 255 [10] Nomoto, K.; Kobayashi, C.; Tominaga, N. Nucleosynthesis in Stars and the Chemical Enrichment of
256 Galaxies. *ARA&A* **2013**, *51*, 457–509.
- 257 [11] Thielemann, F.K.; Argast, D.; Brachwitz, F.; Hix, W.R.; Höflich, P.; Liebendörfer, M.; Martinez-Pinedo, G.;
258 Mezzacappa, A.; Nomoto, K.; Panov, I. Supernova Nucleosynthesis and Galactic Evolution. From Twilight
259 to Highlight: The Physics of Supernovae; Hillebrandt, W.; Leibundgut, B., Eds., 2003, p. 331.
- 260 [12] Greggio, L.; Renzini, A. The binary model for type I supernovae - Theoretical rates. *A&A* **1983**, *118*, 217–222.

- 261 [13] Greggio, L. The rates of type Ia supernovae. I. Analytical formulations. *A&A* **2005**, *441*, 1055–1078,
262 [[astro-ph/0504376](#)].
- 263 [14] Matteucci, F.; Gibson, B.K. Chemical abundances in clusters of galaxies. *A&A* **1995**, *304*, 11,
264 [[astro-ph/9503057](#)].
- 265 [15] Matteucci, F.; Greggio, L. Relative roles of type I and II supernovae in the chemical enrichment of the
266 interstellar gas. *A&A* **1986**, *154*, 279–287.
- 267 [16] Greggio, L. The rates of type Ia supernovae. I. Analytical formulations. *A&A* **2005**, *441*, 1055–1078,
268 [[astro-ph/0504376](#)].
- 269 [17] Bocquet, S.; Saro, A.; Dolag, K.; Mohr, J.J. Halo mass function: baryon impact, fitting formulae, and
270 implications for cluster cosmology. *MNRAS* **2016**, *456*, 2361–2373, [[1502.07357](#)].
- 271 [18] Pollina, G.; Hamaus, N.; Dolag, K.; Weller, J.; Baldi, M.; Moscardini, L. On the linearity of tracer bias
272 around voids. *MNRAS* **2017**, *469*, 787–799, [[1610.06176](#)].
- 273 [19] Teklu, A.F.; Remus, R.S.; Dolag, K.; Beck, A.M.; Burkert, A.; Schmidt, A.S.; Schulze, F.; Steinborn, L.K.
274 Connecting Angular Momentum and Galactic Dynamics: The Complex Interplay between Spin, Mass, and
275 Morphology. *ApJ* **2015**, *812*, 29, [[1503.03501](#)].
- 276 [20] Remus, R.S.; Dolag, K.; Naab, T.; Burkert, A.; Hirschmann, M.; Hoffmann, T.L.; Johansson, P.H. The
277 co-evolution of total density profiles and central dark matter fractions in simulated early-type galaxies.
278 *MNRAS* **2017**, *464*, 3742–3756, [[1603.01619](#)].
- 279 [21] Hirschmann, M.; Dolag, K.; Saro, A.; Bachmann, L.; Borgani, S.; Burkert, A. Cosmological simulations of
280 black hole growth: AGN luminosities and downsizing. *MNRAS* **2014**, *442*, 2304–2324, [[1308.0333](#)].
- 281 [22] Biffi, V.; Planelles, S.; Borgani, S.; Fabjan, D.; Rasia, E.; Murante, G.; Tornatore, L.; Dolag, K.; Granato, G.L.;
282 Gaspari, M.; Beck, A.M. The history of chemical enrichment in the intracluster medium from cosmological
283 simulations. *MNRAS* **2017**, *468*, 531–548, [[1701.08164](#)].
- 284 [23] Santini, P.; others. The evolution of the dust and gas content in galaxies. *A&A* **2014**, *562*, A30, [[1311.3670](#)].
- 285 [24] de Plaa, J.; Werner, N.; Bleeker, J.A.M.; Vink, J.; Kaastra, J.S.; Méndez, M. Constraining supernova models
286 using the hot gas in clusters of galaxies. *A&A* **2007**, *465*, 345–355, [[astro-ph/0701553](#)].
- 287 [25] Teklu, A.F.; Remus, R.S.; Dolag, K.; Burkert, A. The Morphology-Density-Relation: Impact on the Satellite
288 Fraction. *ArXiv e-prints* **2017**, [[1702.06546](#)].
- 289 [26] Sanders, R.L.; others. The MOSDEF Survey: Mass, Metallicity, and Star-formation Rate at $z \sim 2.3$. *ApJ*
290 **2015**, *799*, 138, [[1408.2521](#)].
- 291 [27] Bresolin, F.; others. Young stars and ionized nebulae in M83: comparing chemical abundances at high
292 metallicity. *ArXiv e-prints* **2016**, [[1607.06840](#)].
- 293 [28] González Delgado, R.M.; others. Insights on the Stellar Mass-Metallicity Relation from the CALIFA Survey.
294 *ApJ* **2014**, *791*, L16, [[1407.1315](#)].
- 295 [29] Remus, R.S.; Dolag, K.; Bachmann, L.K.; Beck, A.M.; Burkert, A.; Hirschmann, M.; Teklu, A. Disk Galaxies
296 in the Magneticum Pathfinder Simulations. *Galaxies in 3D across the Universe*; Ziegler, B.L.; Combes, F.;
297 Dannerbauer, H.; Verdugo, M., Eds., 2015, Vol. 309, *IAU Symposium*, pp. 145–148.
- 298 [30] Pastorello, N.; Forbes, D.A.; Foster, C.; Brodie, J.P.; Usher, C.; Romanowsky, A.J.; Strader, J.; Arnold,
299 J.A. The SLUGGS survey: exploring the metallicity gradients of nearby early-type galaxies to large radii.
300 *MNRAS* **2014**, *442*, 1003–1039, [[1405.2338](#)].
- 301 [31] La Barbera, F.; others. SPIDER - VII. Revealing the stellar population content of massive early-type galaxies
302 out to $8R_e$. *MNRAS* **2012**, *426*, 2300–2317, [[1208.0587](#)].